10-14-2024

Cross-Track Seabed Imaging and Buried Object Detection with a Multibeam Sonar

Charles W. Holland
Portland State University

Samuel Pinson
École Navale CC600

Daniel L. Orange
University of California, Santa Cruz

Cody R. Henderson
Norbit, Portland

Citation Details

Holland, C. W., Pinson, S., Orange, D. L., & Henderson, C. R. (2024). Cross-Track Seabed Imaging and Buried Object Detection With a Multibeam Sonar. IEEE Journal of Oceanic Engineering, 1–9. https://doi.org/10.1109/joe.2024.3452134

Cross-Track Seabed Imaging and Buried Object Detection With a Multibeam Sonar

Charles W. Holland, Samuel Pinson, Daniel L. Orange, and Cody R. Henderson

***Abstract*—What lies underneath the ocean floor is of interest to a wide variety of disciplines. The focus here is imaging the upper tens of meters of material beneath the seafloor. The sub-bottom profiler is a valuable tool to that end, producing a 2-D image in depth below the seafloor and along the track of the ship. Geoscientists and engineers are frequently interested in not only the subseabed beneath the ship but also either side or cross-track of the ship. We show an approach to cross-track imaging using a low-frequency multibeam sub-bottom profiler. The main result is the detection of a buried 0.2-m diameter pipeline at a range of nearly 1-km cross-track from the ship in 230-m water depth. This is a swath width coverage of eight times the water depth or nominally an angular range of $\pm 76^\circ$ from nadir. These results have implications not only for buried object detection but also for other potential applications including exploring seabed spatial variability.**

***Index Terms*—Scattering, sediments, sonar detection, sonar equipment.**

I. Introduction

KNOWLEDGE of what lies below the water–sediment interface is important for a wide variety of applications, including understanding the earth's climatic history, marine archaeology, knowing where to place offshore structures such as windfarms, and finding buried unexploded ordnance. The interest here is in imaging the subseabed (both geologic and anthropogenic materials) at high resolution, less than 1 m, down to depths of many tens of meters, and over large areas.

Since geologic processes occur over wide scales of time and space, geologic and geoacoustic properties exhibit wide scales of variability in marine sediments. Seabed spatial variability at many scales is of interest here, but particularly, the geoacoustic mesoscale [1], defined as lateral scales of $O(10^0–10^3)$ m. It is asserted that less is known about these scales than the fine scale (amenable to study using sediment cores and probes) and the large scale (amenable to study using sources and receivers spaced km to tens of km apart).

Received 12 December 2023; revised 11 May 2024 and 6 August 2024; accepted 14 August 2024. *(Corresponding author: Charles W. Holland.)*

Associate Editor: N. Chotiros.

Charles W. Holland is with the Department of Electrical and Computer Engineering, Portland State University, Portland, OR 97201 USA (e-mail: charles.holland@pdx.edu).

Samuel Pinson is with the IRENav EA 3634, BCRM Brest, École Navale CC600, 29240 Brest Cedex 9, France (e-mail: samuelpinson@yahoo.fr).

Daniel L. Orange is with the Department of Earth and Planetary Sciences, University of California, Santa Cruz, Santa Cruz, CA 92037 USA (e-mail: dan@seaseep.com).

Cody R. Henderson is with Norbit, Portland, OR 97232 USA (e-mail: codywh29@gmail.com).

Digital Object Identifier 10.1109/JOE.2024.3452134

Sub-Bottom profiling is a valuable tool for geoscientists and has been under development for more than 6 decades, e.g., [2]. Traditional sub-bottom profiling provides 2-D images of the subseabed in time (which can be converted to depth if the sound speed is known) and along-track distance. An example is shown in Fig. 1, which shows finely laminated sediment in the upper 20 m, with a stronger amplitude sub-bottom horizon ∼20 m below the seafloor.

While these data are highly informative, to better understand the mesoscale, it is needful to know how the seabed changes laterally (cross track) from the 2-D along-track image.

Further, a sub-bottom profile typically contains little information about small-scale scattering (scales much smaller than the Fresnel zone) from layer boundaries or from heterogeneities within the sediment, including both geologic and anthropogenic materials.

Synthetic aperture sonar (SAS) is another valuable tool, in particular for cross-track target detection at frequencies typically in the tens of kilohertz where the sonar system transits close to the seabed, e.g., as presented in [3], [4], and [5]. While SAS has been extremely successful, for some applications, a low-frequency multibeam sonar may be a useful alternative (e.g., deeper sediment penetration and/or larger coverage rates at water depths greater than the inner continental shelf). The objective of this work is to image the sub-bottom in the cross-track direction using a multibeam sonar.

The remainder of this article is arranged as follows. Section II describes the approach. The results are provided in Section III, where it is shown that cross-track imaging with a multibeam sonar is possible out to at least four water depths or a nominal angle of $\pm 76^\circ$ from nadir. In particular, a buried 0.22-m-diameter pipeline is detected out to ranges of 920 m in 230-m water depth. This is the main result of this article and it, to our knowledge, has not been previously achieved with a multibeam sonar. Section IV contains some details including the factors that govern pipeline detectability. It also discusses potential applications beyond object detection. For example, cross-track imaging can possibly provide useful information about seabed spatial variability at the geoacoustic mesoscale. Finally, Section V concludes this article.

II. Approach

The Kongsberg SBP120 [6] and more recent SBP29 are multibeam sub-bottom profilers that provide high-quality along-track sub-bottom profiles. There is a manufacturer's option to view

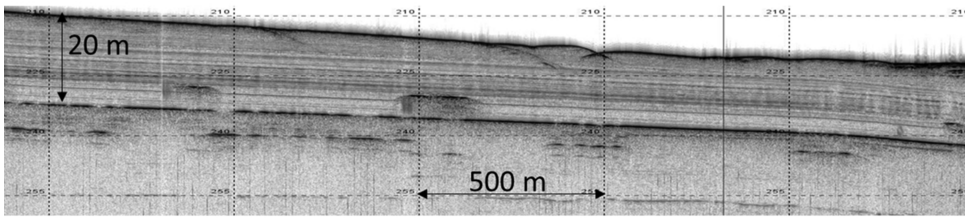

Fig. 1. Sub-Bottom profile from the Santa Barbara Channel. The vertical exaggeration is 11:1 [see Fig. 3(b) for location].

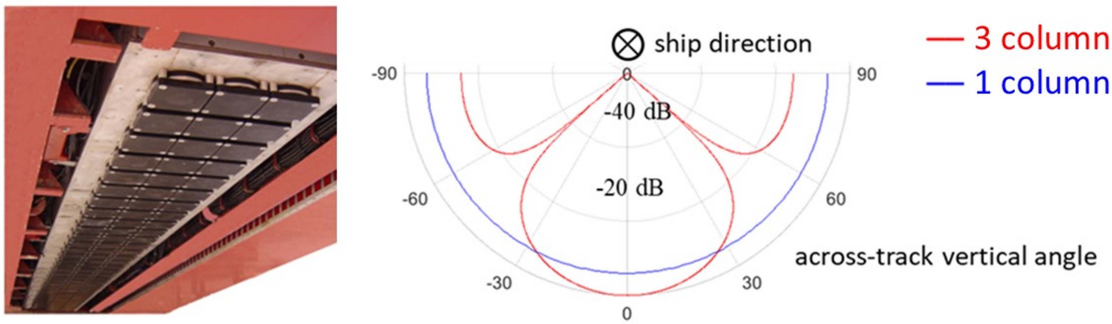

(a) (b)

Fig. 2. Kongsberg SBP (a) transmitter showing the three columns of 32 transducers (photo courtesy of Bjørnar Llangli and Kongsberg) where the outer two columns are designed to operate at $1/2$ power. The transmitter is mounted on the ship along-track, which gives (b) theoretical cross-track beampattern at 4 kHz for the three columns (—) and the central column (—) with the outer elements clamped. The single column is much better suited for cross-track imaging.

cross-track beam time series, which follow a parabola in the cross-track direction for a single ping. However, those data can often be difficult to interpret. While Kongsberg explored cross-track buried object detection [6], the cross-track beams are limited to near nadir, $\pm 15°$ of nadir or within ¼ of the water depth on either side of the ship. As an indication of the difficulty in using the cross-track information, users, to our knowledge, over the last several decades of its existence have nearly exclusively employed the sonar for along-track profiles.

The SBP29 source consists of three 7-m-long columns mounted on the hull of the ship lengthwise [see Fig. 2(a)]. Each column has 32 elements, with a frequency band of 2−9 kHz. The receiver is mounted orthogonally and is 3.528 m wide (on the vessel employed here) with 64 equally spaced elements.

In the original SBP120 configuration [6], with a frequency band of 2.5–7 kHz, there were 2 hurdles that prevented full cross-track imaging: 1) the only cross-track information was within ¼ of the water depth on either side of the ship; and 2) transmitting from the 3 columns led to a beampattern with deep frequency-dependent nulls in the cross-track direction [see Fig. 2(b) (red curve)]. To remove these hurdles, we requested the manufacturer to provide the element-level time series data and provide an option to transmit from just the center column of the transmitter. The former gives the user the option to perform their own beamforming; the latter provides a nearly omnidirectional beam cross-track [see Fig. 2(b) (blue line)]. These two modifications were made, and the SBP29 was installed on the *R/V SALLY RIDE* and tested at-sea in June 2021.

III. Cross-Track Imaging

The first science experiment conducted with the single-column transmitter and element-level time series, entitled *SeaBed Properties Exploration & Experimentation (SBPex2022)*, in the California Continental Borderland offshore southern California during August to September 2022. One of its objectives was to explore the potential of cross-track imaging. A useful way to determine the cross-track imaging limits is to test it against targets of opportunity. To this end, a site was selected near three buried pipelines in the Santa Barbara Channel [see Fig. 3(a)]. The pipelines are a few hundred meters apart and are likely identical. Following the experiment, an offshore company provided information about the pipeline: burial depth, 1 m when laid; diameter, 0.22 m; and wall thickness, 0.01 m. The three pipelines are made of carbon steel; two carry oil and one natural gas. Which pipeline carries gas is not known.

The ship track was designed with four parallel lines [see Fig. 3(b)] with the closest, Line 1, a few hundred meters away from the nearest pipeline (pipeline A) and ∼600 m from the furthest (pipeline C). Relative to Line 1, the other three Lines are at increasing distances of 50, 150, and 320 m from the pipelines. Line 2 and Line 1 have such a similar offset from the pipelines, that only Lines 1, 3, and 4 are reported here. Water depth varies slightly over the area, with somewhat shallower depths at the pipelines (as shallow as 218 m at the furthest pipeline looking broadside from the start of Line 1). The seabed slope from the ship to the pipelines is small, less than ∼1°.

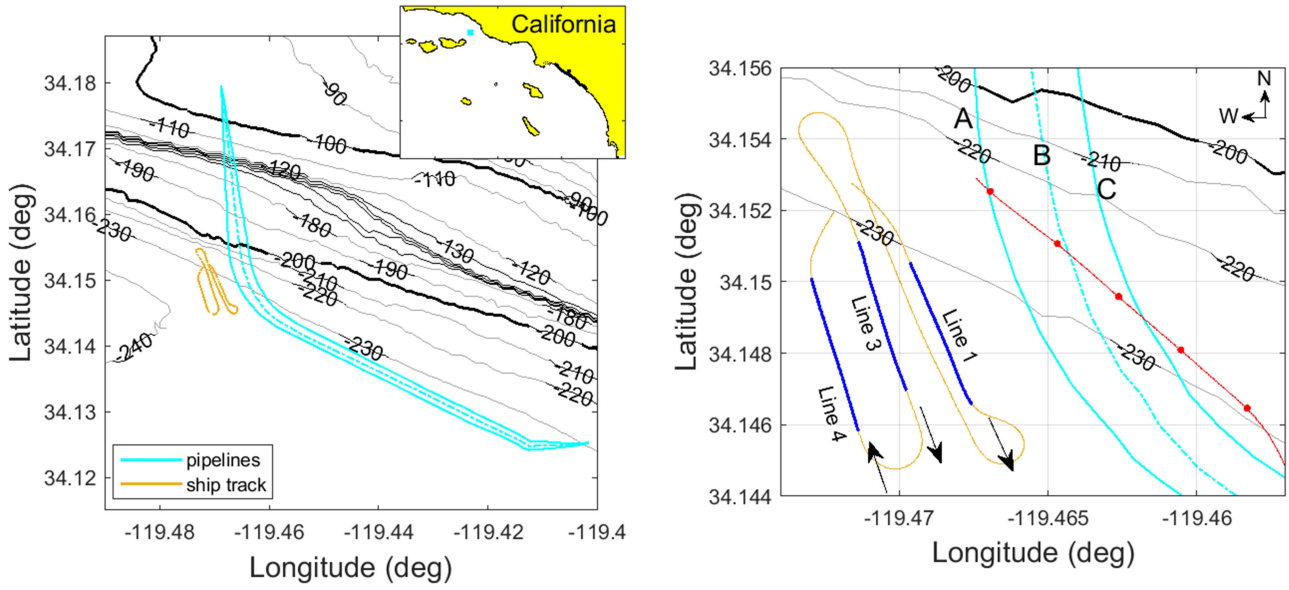

(a) (b)

Fig. 3. (a) Southern California region showing the pipeline locations (cyan lines) and ship tracks (gold lines). The inset shows the experiment location (■) within the Santa Barbara Channel. (b) Zoom-in showing the three lines discussed in the text with arrows showing ship direction. The location (—●—) of the sub-bottom profile in Fig. 1 is also shown with the track direction from northwest to southeast; the dots correspond to the dashed vertical time marks in Fig. 1. The sub-bottom profile track provides useful context for the cross-track look directions from Lines 1−4. The bathymetric contours are in meters.

The ship's speed was 4 kn with a pulse repetition interval of 4 s. The projected signal was an 80-ms linear frequency modulated (LFM) pulse from 2–9 kHz using the single transmit column with 16 of the 32 transducers (an along-track beamwidth of ∼6° at 4 kHz). The far field of this aperture is 74 m at 9 kHz, thus all the pipelines are in the far field of the transmitter at all frequencies, along all lines.

The cross-track image intensity (e.g., see [7] and [8]) is formed for a given ping on a 2-D grid broadside to the ship, using spherical wave beamforming

$$I(\boldsymbol{r}) = \left| \sum_{n=1}^{N} p_n^{\mathcal{H}}\left(\tau_n(\boldsymbol{r})\right) \right|^2 \tag{1}$$

where n is the receiver element index ($N = 64$), p_n are match filtered measured time series, $\mathcal{H}$ indicates the analytic signal using a Hilbert transform, and τ_n is the travel time from source to grid point position $\boldsymbol{r}$ and back to the receiver element n. The data are corrected for roll, and no other compensation is applied. The cross-track image at this stage of the processing for a single ping on Line 1 is shown in Fig. 4(a) where the ship ($\otimes$) is traveling into the page so that the starboard is to the right (positive ranges) and port is to the left (negative ranges). The 2-D grid in polar coordinates has a range resolution of 0.2 m and azimuthal resolution of 0.1°. The seabed is indicated by the dotted brown line and the normal incidence seabed reflection is clearly seen beneath the ship at 0-m range. There is a second reflection 20 m below the water–sediment interface which corresponds to the sub-bottom layer observed in the along-track image (see Fig. 1). This doublet occurs again at about twice the water depth, due to the signal traveling from the source to the bottom to sea surface to bottom to receiver. It is termed the first multiple.

One of the most prominent features in the image is the high sidelobes (along a constant radius from the source) from each strong arrival. The sidelobes are problematic for imaging, especially from the first multiple, because they obscure features in the seabed that may be present. The sidelobes can be significantly diminished by computing the coherence factor [9], [10]

$$\mathrm{CF}(\boldsymbol{r}) = \frac{\left|\sum p_n^{\mathcal{H}}\left(\tau_n(\boldsymbol{r})\right)\right|^2}{\sum \left|p_n^{\mathcal{H}}\left(\tau_n(\boldsymbol{r})\right)\right|^2} \tag{2}$$

where the summation sign is over receiver number $n = [1\ N]$ as in (1). In this article, CF is smoothed with a seven-point Hann window in the polar range coordinate. The coherence factor has a range from 0 to 1. When there are many random scatterers within a 3-D resolution cell, the scattered wavefield tends toward being incoherent (random phase) resulting in a low CF. For a single coherent scatterer in a resolution cell, such as a discrete object in a low-noise background, CF tends to be high (e.g., as in [10]). The resolution cell is a section of a spherical shell whose thickness is governed by the pulse resolution, width by the transmit beamwidth, and height by the receiver aperture. The volume of the spherical shell is the smallest at the nadir and increases with range. Thus, if random scatterers were distributed uniformly throughout the area, CF would be highest (but still low) near the nadir and would tend toward zero at large ranges (where the volume is largest). CF for a discrete object would tend to be highest near the nadir and decrease with increasing range due to the increase in the number of random scatterers within

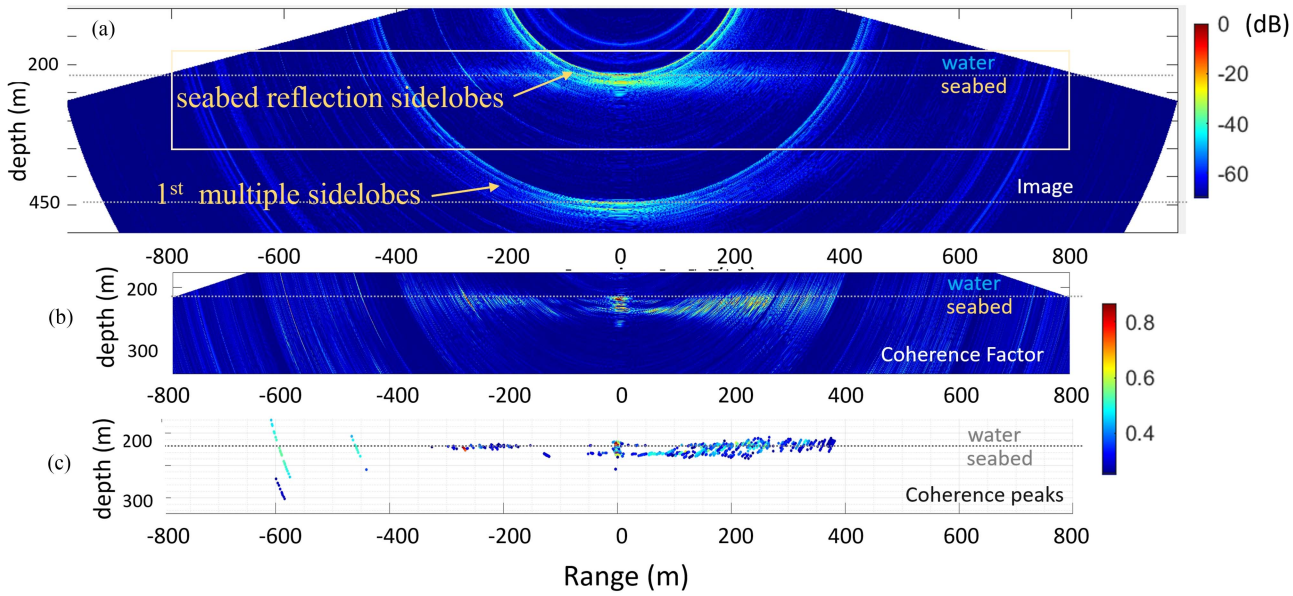

Fig. 4. Cross-track imaging for a single ping. (a) Image formed using (1), with the white box indicating the spatial limits for the following subplots. (b) Coherence factor. (c) Coherence peaks. The water–seabed interface is indicated by the dotted brown line, where all depths are relative to the source and receiver transducers that are ∼5 m below the sea surface.

the cell. However, this assumes that the random scatterers are uniformly distributed across the region, which may not be true.

The coherence factor for this ping is shown in Fig. 4(b) where a significant reduction in the sidelobes is apparent. Information about features on and under the seafloor is further enhanced by thresholding the coherence factor and taking local peak values. Here, a threshold value was set to 0.25, and peak values were obtained with the MATLAB function imregionalmax.m [11]. The local peaks of the coherence factor, hereafter called the coherence peaks, are shown in Fig. 4(c), indicating the locations of the strongest coherent scatterers on and below the seafloor.

To better understand the spatial relationship between the cross-track data and the pipelines, a zoom-in image of the ship tracks in rotated coordinates is shown in Fig. 5 where the port side of the ship is to the left—in the same orientation as the cross-track data of Fig. 4.

Fig. 6 shows the coherence factor and the coherence peaks for the same ping as in Fig. 4 with added annotations. On the port (left) side, three strong returns are clearly seen at horizontal ranges of about 275, 460, and 600 m. These can be seen in both the coherence factor and the coherence peaks but are most easily seen in the coherence peaks. The horizontal ranges with high coherence agree closely with the pipelines' reported positions.

The results from Line 1 clearly show the ability to detect the buried pipelines out to ranges of 600 m. Data from further ranges, Lines 3 and 4, are now examined. On Line 3 [see Fig. 3(b)], the range from ship to farthest pipeline is ∼750 m (pipeline C). The coherence peaks are shown in Fig. 7 (top), where the pipeline is clearly seen at −750 m at a high coherence value. On Line 4, the range from the ship to the farthest pipeline is 920 m and the data also exhibit a clear detection. The data for Lines 3 and 4

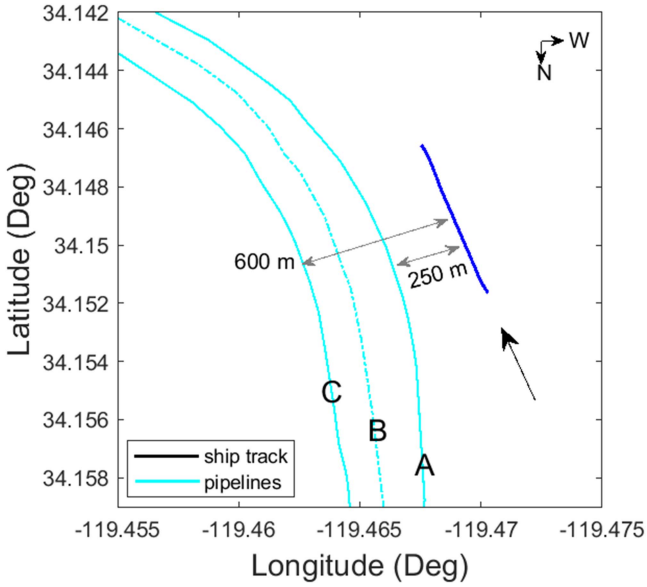

Fig. 5. Line 1 ship track and three pipelines mapped for convenience so that the port side of the vessel is to the left. The direction of the black arrow indicates ship direction and approximate distances are indicated.

were processed and displayed identically to that for Line 1 (see Fig. 6).

The main result of this article is that using cross-track imaging, a 0.22-m-diameter pipe, buried 1 m in the seabed, can be detected with a multibeam sonar out to horizontal ranges of 920 m in 230-m water depth, i.e., at four times the water depth, or equivalently at 76° from nadir (assuming straight line paths).

The rest of this article discusses some details of the result, including some of the key underlying physics.

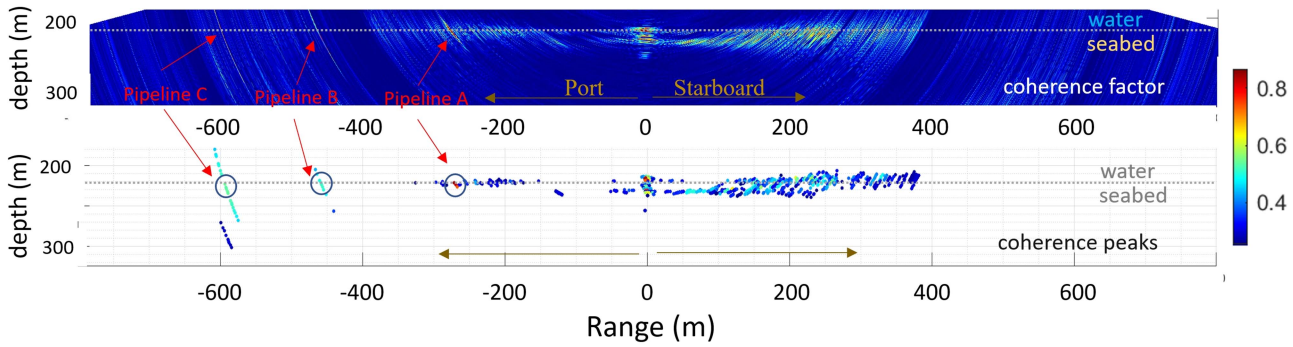

Fig. 6. Cross-track imaging for the same ping as Fig. 4(b) and (c) with added annotations for pipeline detections.

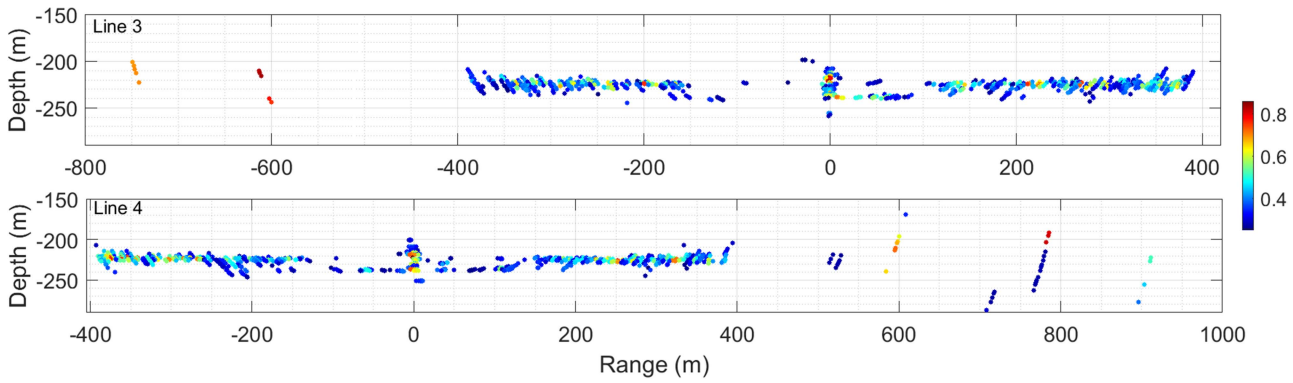

Fig. 7. Cross-track imaging coherence peaks for pings from Line 3 (top) where the pipelines are on the port side (negative ranges) and Line 4 (bottom) where the pipelines are on the starboard side (positive ranges).

IV. Discussion

In this section, several aspects of the results are explored, including factors that govern pipeline detectability, the spatial resolution of the cross-track data, the spatial persistence of pipeline detections, differences in along-track and cross-track physics, and additional possible applications.

A. Pipeline Detectability

Some considerations are briefly discussed to understand why the detections are possible. Classical scattering theory dictates that the scattering strength from a circular cylinder is a function of the nondimensional product $ka\sin\phi$, where k is the acoustic wave number, a is the radius, and ϕ is the horizontal angle between the incoming wave and the cylinder axis (i.e., $\phi = 90°$ at broadside). At frequencies below $ka\sin\phi = 1$, the scattered intensity drops very rapidly, $(ka)^{-4}$, as first shown by Rayleigh [12]. At high frequencies, $ka\sin\phi > 1$, the scattering strength increases as $(ka)^j$ where $j = 1$ for a perfectly straight cylinder, and $j = 0$ for a curved or nonuniform cylinder [13]. This regime is often termed the geometric scattering region. For these pipelines, $a = 0.11$ m, and the interrogating LFM pulse leads to $0.9 < ka\sin\phi < 4$. Thus, most of the pulse spectral energy is in the geometric scattering regime, where the highest scattering strength occurs.

Another factor controlling the detectability of buried objects is the sediment's geoacoustic properties, especially the sound speed and compressional wave attenuation. The sediments in the upper 20 m are Holocene (recent) and originate from the Santa Clara River [14]; the laminations in the upper 20 m as shown in Fig. 1 are believed to arise from increased silt (i.e., larger grains) input from winter flooding events [15]. Of importance to this work, the sediments are known to be fine-grained (muddy), and muddy sediments generally exhibit a sound speed less than that of water and a low compressional attenuation. The low sound speed and attenuation both enhance detectability and are briefly discussed in the paragraphs below.

A sediment sound speed lower than water means that the grazing angle of refraction into the sediment is greater than the grazing angle in the water column. This leads to a shorter path length in the sediment than if the sediment sound speed were the same or higher than that of the water—especially at lower grazing angles.

Marine sediments have a much larger attenuation than that of the water column. For example at 5 kHz, the seawater attenuation is about 3×10^{-4} dB/m [16], whereas silts typically have an attenuation of about 3 dB/m [17], i.e., four orders of magnitude larger than seawater. For muddy sediments, one study suggests that the attenuation is less than $\sim$0.15 dB/m [18] at 5 kHz. This relatively low attenuation over the short distances involved here leads to small losses in the acoustic field. For example, assuming a mud sound speed ratio of 0.98, at the furthest offset the two-way path length in the sediment is 5 m and the total sediment attenuation loss at 5 kHz is 0.75 dB. At shorter source–receiver

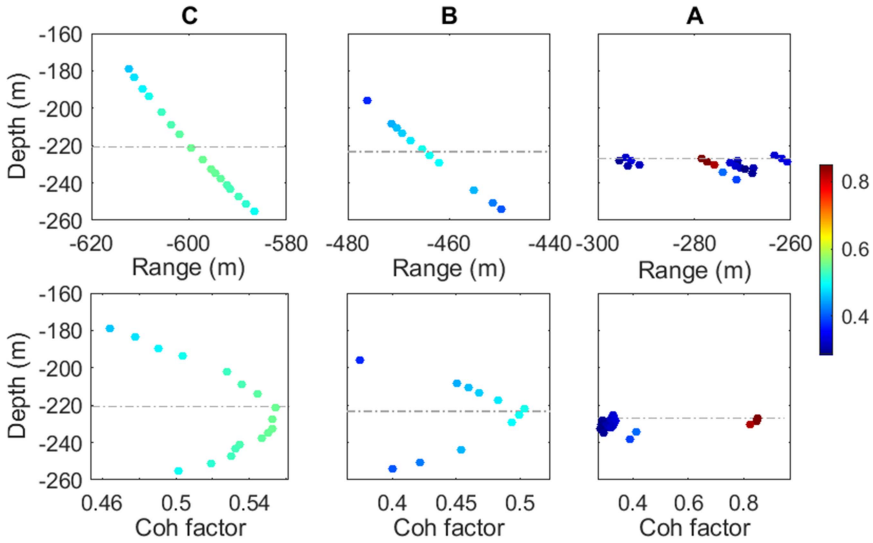

Fig. 8. Three columns show detections at pipelines A, B, and C for a ping on Line 1. The seabed is shown by the gray dashed line. Top row: MLH as a function of range. Bottom row; MLH as a function of coherence factor. The maxima of MLH are near/at the seabed as expected.

offsets, the path lengths and hence the total attenuation would be smaller.

Another important factor governing the pipeline detectability is the near omnidirectional behavior associated with using the central transmit column, since the detections span a range of source grazing angles, i.e., 7°–37° (accounting for refraction).

B. Simplifications

For simplicity, the cross-track data were processed using an isospeed ocean, where the sound-speed profile is required to convert travel time to position in (1–2). However, the measured sound-speed profile has an 8-m sea surface mixed layer with a sound speed of 1522 m/s; at the water–sediment interface, the water sound speed is 1490 m/s. This means that the absolute geographic positions may not be quite correct. However, modeling shows that the isospeed assumption in the water column leads to horizontal errors of less than $\sim$1 m at the water–sediment interface out to ranges of 1000 m. The effects of sediment refraction are also small here because the burial depth of 1 m is a small fraction of the water depth. Its effect leads to errors of less than 1 m in horizontal offset.

In other environments, where sub-bottom features of interest are at sediment depths greater than $\sim 1/4$ of the water depth, the difference between the water column and sediment speeds may give rise to non-negligible sediment refraction effects. In that case, the interval velocity (harmonic average of the sediment sound-speed profile) can be estimated directly from the coherence factor [8]. With the interval velocity obtained, the imaging can be performed such that the position of the sub-bottom feature is correctly positioned in depth and range.

C. Spatial Resolution of the Coherence Peaks

The pipeline detections exhibit wide arcs at far ranges, for example, in Fig. 4(c). The arcs are portions of a circle with the source at the center. They are high values of the coherence factor on the main lobe of the beam striking the pipeline and are termed main lobe highlights (MLH).

For ease of discussion, MLH details from a ping on Line 1 are shown in Fig. 8 (top row). In a noise-free image, MLH would not exist. The peak picking function (imregionalmax) finds regional maxima in an image that are connected components of pixels with a constant intensity value, surrounded by pixels with a lower value. "regional maxima" is a single pixel when all adjacent pixels have a lower value. For example, imregionalmax applied to a Hanning function would yield a single value at its peak. However, if noise is added, then "local" peaks separated by small valleys may exist on the flanks. Thus, MLH persist in the data because the coherence factor fluctuates in amplitude along the main lobe arc. This can be seen most clearly in Fig. 8 for pipelines B and C, where the coherence factor decays in a broad lobe in azimuth (top row) and amplitude (bottom row) away from its peak value.

It is important to note that although the MLH are visually distracting, it is clear that the scattering object (pipeline) is at or near the peak amplitude of the MLH. This is shown most clearly in Fig. 8 (bottom row). From left to right, the peak coherence factor at pipeline C is the one closest to the seabed; for pipeline B, the seabed falls between the two highest values; and for pipeline A, the peak is near/at the seabed. Thus, the location of the object can be estimated by taking the maximum value of the coherence factor along the main lobe, or alternatively fitting a function to the main lobe and taking its peak value. This has not been done here.

D. Coherence Factor Spatial Persistence

In Section III, the cross-track imaging was described and illustrated with a single ping from Lines 1, 3, and 4. It is of interest to understand how the results evolve from ping to ping. This is shown for the 56 pings along Line 1 (see Fig. 9), where the colored circles indicate returns above the threshold. For convenience in this analysis, the threshold is set to 0.4.

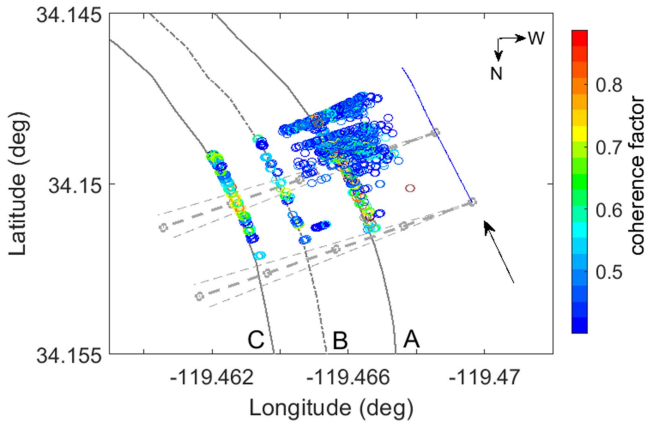

Fig. 9. Coherence peaks from 56 pings of data (colored circles) for Line 1 (see [5, Fig. 3(b)]). The broadside beam directions (– –O– –) and 3-dB beamwidths (_ _ _) are shown at 2-min intervals. The gray circles on the broadside beam indicate ranges at 200, 400, 600, and 800 m. The ship track is shown in blue.

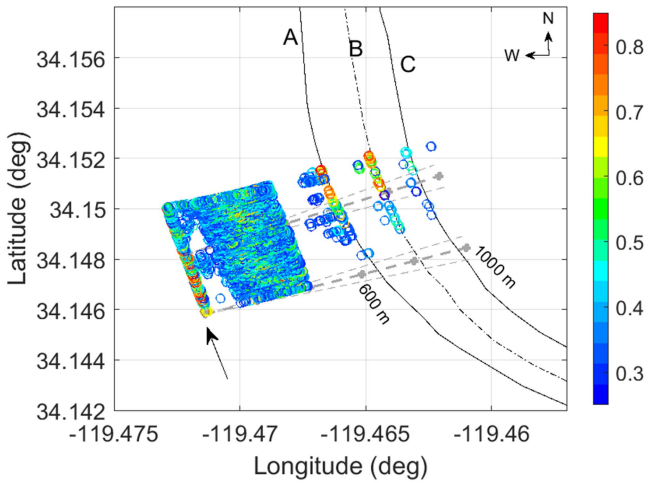

Fig. 10. Coherence peaks from 56 pings of data (colored circles) for Line 4 [see Fig. 3(b)]. The broadside beam directions (– –O– –) and beamwidths (_ _ _) are shown at 2-min intervals. The gray circles on the broadside beam indicate ranges at 200, 400, 600, 800, and 1000 m.

In the first half of the track, all three pipelines are easily distinguished above the background "noise" (due to sediment scattering). Although in the latter half of the track, pipelines B and C are still easily distinguished, numerous coherence values above the threshold appear at locations around pipeline A. These are generally at a low coherence value so that in some, but not all, instances, using the highest value of the coherence in that range window (200–400 m) yields the correct pipeline position. One example of this is shown in Figs. 4 and 8 where numerous coherence values above the threshold can be seen near pipeline A, but the highest coherence factor is clearly associated with the pipeline.

What causes the change in the background sediment scattering? Presumably a change in the sediment properties. In principle, the background "noise" could come from scattering from the water–sediment interface, the 20-m sub-bottom interface, or scattering from within the sediment volume. In this environment, it seems clear from inspection of Fig. 6(a) that on the starboard side (positive ranges), scattering arises principally from the water–sediment and sub-bottom interfaces. On the port side, the water–sediment interface contributions dominate.

Why does the background noise (scattering levels) not increase around pipelines B and C as they do around A? One explanation is the difference in grazing angles at A, B, and C, which are 40°, 25°, and 20°, respectively. Thus, scattering from the water–sediment (or sub-bottom layer) interface should be lower at pipelines B and C than that at A since interface scattering decreases with decreasing angle. At these angles, the interface scattering strength decrease could be bracketed by a factor of $\sin^m(\theta)$, where typically $1 \leq m \leq 4$, below say 60°. Thus, sediment interface scattering is smaller at increasing range and this may explain why detections at B and C have fewer competing coherence peaks than at A on the latter half of the track.

Detection persistence is also shown at the farthest range, which is along Line 4 (see Fig. 10). Here, pipeline detections are rare in the early part of the track, but later in the track, all pipelines out to 920 m are regularly detected. The simplest explanation is the change in the horizontal angle between the ship heading and the pipelines. For example, pipeline C changes 20° throughout this run. At the beginning of the run (southern end), the difference in ship and pipeline heading is ∼15°. The headings are the same near the end of the run, i.e., the pipeline is near broadside. Thus, as expected, the highest detection persistence is observed near the end of the run, at broadside. In addition, note the increase of the coherence factor amplitude at all pipelines toward the end of the run.

We can further examine the effect of heading differences on detection by returning to the results for Line 1 (see Fig. 9). On this run, pipeline C heading also varies by ∼20°. At the beginning of the run, the ship and pipeline heading differs by ∼12° passing through broadside at ∼2/3 through the run and ending the run with a heading difference of ∼6°. As expected, note that pipeline C detections are fewer near the beginning of the run than at the end, indicating that horizontal angles closer to broadside yield stronger returns.

It may be questioned whether 920 m is the absolute limit of pipeline detection range for this environment. Given the detection persistence at 920 m, it is likely that farther detection ranges are possible. However, no other data are yet available to answer that question definitively.

E. Differences in Physics Governing Along- and Cross-Track Data

We have demonstrated the ability to image the subseabed cross-track. It is clear, though, that the information is different in each direction. The along-track and cross-track data are governed by different physics and therefore by different processes.

The along-track data are dominated by specular reflection from sediment layer interfaces. Thus, the sediment layer morphologies are generally easily observed. The reflection amplitude from a given interface is generally indicative of the impedance change between the media above and below it. These data are highly informative to geologists and other geoscientists for determining the formative geologic processes, such as deposition and erosion, in a chronological framework. On the

other hand, the data have relatively low information content on small-scale scatterers, especially if they reside near a sedimentary boundary.

The cross-track data by contrast are governed by scattering and contain information about small-scale scatterers embedded in the sediment. These can include geologic or anthropogenic objects such as gas pockets, unexploded ordinance, or pipelines. These data could potentially serve academia, industry, marine archeology as well as other communities. On the other hand, the cross-track data have less information about layer boundaries since there is only a scattered field and no reflected field. The scattered field from a boundary: 1) can *only* exist where there is both an impedance change and sufficient roughness at the spatial wave numbers corresponding to the Bragg condition (a function of the frequency and angle); and 2) becomes very small at low grazing angles, and thus can only be observed at sufficiently steep grazing angles. In cases where these conditions are met, the scattered field from a given interface inherently fluctuates in amplitude and arrival time, leading to sometimes spatially "fuzzy" boundaries (e.g., see cross-track ranges 100–400 m, Fig. 6).

Finally, we note one other difference between along-track and cross-track data; for a single ping, the along-track sub-bottom profile is 1-D, whereas the cross-track data are 2-D.

The differences can be summarized as follows.

1) Along-track data contain significant information on the sub-bottom layered structure. Huge volumes of data and many decades of research by academia and industry have led to valuable, well-established methods of interpretation of such data, e.g., the pioneering work in [19]. On the other hand, small-scale embedded scatterers are more difficult to detect, in part because the layer boundary reflections mask them.
2) Cross-track data contain significant information on small-scale scatterers. While progress has been made in terms of understanding seabed scattering, e.g., [20], the relative amount of data examined and the interpretive methods are much less developed than the along-track counterparts.

F. Possible Applications

One message of the article is that is possible to image the subseabed in the cross-track direction using a low-frequency multibeam sonar. By subseabed image here we mean an image of the subseabed without prejudice to material, whether they be natural (e.g., sediments and gas) or anthropogenic. The demonstration of cross-track imaging was facilitated by the detection of small-diameter buried pipelines. While detecting sub-bottom objects is of significant interest in its own right, it is important to note that even broader applications are possible. Additional applications of cross-track imaging could include improved characterization of many aspects of the subseabed environment.

What was considered as "background noise" for detection, may be a useful signal for other applications. The cross-track data contain significant information about seabed scattering. As one example in the field of sediment acoustics, the data may be useful in determining the dominant scattering mechanisms in a particular environment, whether from layer interface roughness or sediment volume heterogeneities. In the seabed environment explored here, it appears that roughness from the water–sediment interface and the layer 20-m sub-bottom are dominant [see Fig. 4(c) from 0 m to 250 m (Line 1)]. From 0 m to 100 m, the sub-bottom layer exhibits the highest coherence factor. From 100 m to 250 m, both the water–sediment and sub-bottom interfaces exhibit comparable coherence. Although sometimes MLH overlap or nearly overlap, it seems likely from inspection that the likely dominant scattering mechanisms are roughness at the two interfaces and that scattering from volume heterogeneities between the two interfaces is less important. Continued progress on reducing MLH should be able to better resolve the layers. These data are sensitive to, or equivalently provide information about, sediment roughness at horizontal scales of 0.1–2 m (associated with the Bragg wave number), which includes scales at the geoacoustic mesoscale [1].

As another example of detecting variability at the mesoscale, consider Fig. 9, where, in the latter half of the track, there is a clear change in the coherence factor near pipeline A. Over scales of tens of meters, CF increases about halfway through the track. This change may be related to a change in impedance or roughness spectra or both. Evidence of spatial variability may also be evident in Fig. 4(c), where CF is different at the same absolute ranges port or starboard. Fig. 10 also contains intriguing variability, where a spatial "window" of low CF close to the source changes along the track.

It should be noted that the CF detection performance in (2) is a ratio of the coherent and incoherent pressure sums. However, for simplicity, Section IV discusses the effects of the scattering strength of the pipeline and sediment, but only in relation to the image intensity (numerator). To fully explain the CF behavior, a more involved analysis is required, which is beyond the scope of the present work.

Finally, while the coherence factor was chosen for imaging here, other quantities could be used. As one example, the image intensity could be used at coherence peak locations. Depending on the application, other quantities may have a higher information content for the particular sediment property of interest.

V. Summary

Cross-track imaging from a multibeam sonar was demonstrated by detecting a buried 0.22-m-diameter pipeline for the span of pipeline cross-track ranges during the experiment, from 250 to 920 m in 230-m water depth. This is clearly a significant result relative to detecting buried objects. The key enabling aspects include access to the raw time series, the ability to transmit with a single column, which yields a nearly omnidirectional cross-track beam, and advanced imaging methods.

These results have implications not only for buried object detection but also for a wide range of other applications. One of these is addressing the scientific question of how sediments in the upper tens of meters vary laterally at scales from $O(10^0 - 10^3)$ m, i.e., the geoacoustic mesoscale. These are scales of variability that traditionally have been difficult (i.e., expensive) to measure over large areas. Since the equipment used here is hull-mounted, i.e., no towed receivers or sources are required, this work can lead to mapping and understanding the subseabed variability at unprecedented scales.

ACKNOWLEDGMENT

The authors acknowledge the support of the Office of Naval Research, Littoral Geosciences and Optics with Dr. Reginald Beach as a program manager. The authors would like to thank Bjørnar Langli of Kongsberg for his expertise and responsiveness in the SBP29 modifications and the captain, crew, and marine technicians of the *R/V "SALLY RIDE"* for their flexibility and able handling of the ship during survey operations. The authors would also like to thank Jon Wallace, Chevron, for information on the imaged pipelines.

REFERENCES

[1] C. W. Holland, P. L. Nielsen, J. Dettmer, and S. E. Dosso, "Resolving meso-scale seabed variability using reflection measurements from an autonomous underwater vehicle," *J. Acoust. Soc. Amer.*, vol. 131, pp. 1066–1078, 2012.

[2] H. E. Edgerton and H. Payson, "Sediment penetration with a short-pulse sonar," *J. Sedimentary Res.*, vol. 35, pp. 876–880, 1965.

[3] J. E. Piper, K. W. Commander, E. I. Thorsos, and K. L. Williams, "Detection of buried targets using a synthetic aperture sonar," *IEEE J. Ocean. Eng.*, vol. 27, no. 3, pp. 495–504, Jul. 2002.

[4] S. G. Schock, "Synthetic aperture 3D buried object imaging," *Int. J. Soc. Underwater Technol.*, vol. 27, no. 4, pp. 185–193, 2008.

[5] J. E. Piper, R. Lim, E. I. Thorsos, and K. L. Williams, "Buried sphere detection using a synthetic aperture sonar," *IEEE J. Ocean. Eng.*, vol. 34, no. 4, pp. 485–494, Oct. 2009.

[6] B. Langli and J.-C. Le Gac, "The first results with a new multibeam subbottom profiler," in *Proc. MTS/IEEE Techno-Ocean*, 2004, vol. 2, pp. 1147–1153.

[7] S. Pinson, C. W. Holland, and Y. Stephan, "Roughness influence on multibeam-subbottom-profiler specular echoes and roughness parameter inversion," *J. Acoust. Soc. Amer.*, vol. 143, pp. 2622–2631, 2018.

[8] C. W. Holland and S. Pinson, "Sediment interval velocities from a monostatic multibeam sonar," *J. Acoust. Soc. Amer.*, vol. 147, pp. EL13–EL18, 2020.

[9] N. Niedell and M. Taner, "Semblance and other coherency measures for multichannel data," *Geophysics*, vol. 36, pp. 482–497, 1971.

[10] A. E. A. Blomberg, T. C. Weber, and A. Austeng, "Improved visualization of hydroacoustic plumes using the split-beam aperture coherence," *Sensors*, vol. 18, no. 7, 2018, Art. no. 2033.

[11] The MathWorks, Inc., "MatLab image processing toolbox version 11.2 (R2020b)," Natick, MatLab version: 9.9 (R2020b), 2020. [Online]. Available: https://www.mathworks.com

[12] J. W. S. Rayleigh, *The Theory of Sound*, 2nd ed., vol. 2. New York, NY, USA: Dover, 1945.

[13] T. K. Stanton, "Simple approximate formulas for backscattering of sound by spherical and elongated objects," *J. Acoust. Soc. Amer.*, vol. 86, pp. 1499–1510, 1989.

[14] P. Fleischer, "Mineralogy and sedimentation history, Santa Barbara Basin, California," *J. Sedimentary Petrology*, vol. 42, pp. 49–58, 1972.

[15] X. Du, I. Hendy, and A. Schimmelmann, "A 9000-year flood history for Southern California: A revised stratigraphy of varved sediments in Santa Barbara Basin," *Mar. Geol.*, vol. 397, pp. 29–42, 2018.

[16] R. E. Francois and G. R. Garrison, "Sound absorption based on ocean measurements. Part II: Boric acid contribution and equation for total absorption," *J. Acoust. Soc. Amer.*, vol. 72, pp. 1879–1890, 1982.

[17] E. L. Hamilton, "Geoacoustic modeling of the sea floor," *J. Acoust. Soc. Amer.*, vol. 68, pp. 1313–1340, 1980.

[18] F. A. Bowles, "Observations on attenuation and shear-wave velocity in fine-grained, marine sediments," *J. Acoust. Soc. Amer.*, vol. 101, pp. 3385–3397, 1997.

[19] P. R. Vail and R. M. Mitchum Jr., "Seismic stratigraphy and global changes of sea level: Part 1. Overview: Section 2. Application of seismic reflection configuration to stratigraphic interpretation," in *Seismic Stratigraphy – Applications to Hydrocarbon Exploration*. Tulsa, Oklahoma, USA: American Assoc. Petroleum Geol., 1977.

[20] D. Jackson and M. Richardson, *High-Frequency Seafloor Acoustics*. Berlin, Germany: Springer-Verlag, 2007.

Charles W. Holland received the B.S. degree in engineering from the University of Hartford, West Hartford, CT, USA, in 1983, and the M.S. and Ph.D. degrees in acoustics from The Pennsylvania State University, State College, PA, USA, in 1985 and 1991, respectively.

His Ph.D. thesis addressed acoustic propagation through and interface waves in poroviscoelastic marine sediments. From 1985 to 1996, he conducted research in ocean and sediment acoustics with Planning Systems Inc., Reston, VA, USA. In 1996, he joined the NATO Undersea Research Centre, La Spezia, Italy, where he developed seabed reflection and scattering measurement and geoacoustic estimation techniques. In 2001, he joined the Applied Research Laboratory, The Pennsylvania State University, and in 2020, he joined the Portland State University where he continues his research in both theoretical and experimental aspects of ocean waveguide and seafloor acoustics. His contributions to this work include concept generation, experiment design, data collection, data processing, theoretical analysis, and manuscript preparation and editing.

Dr. Holland is a Fellow of the *Acoustical Society of America*.

Samuel Pinson received the Engineer's degree in acoustics and vibration from ENSIM, Le Mans, France, the M.S. degree in mechanics and acoustics from the Université du Maine, Le Mans, France, both in 2007, and the Ph.D. degree in underwater acoustics from the Université de Bretagne Occidentale, Brest, France, in 2011.

After his Ph.D. degree, he continued his research on sediment acoustics through various postdoctoral positions. Since 2021, he has been a Teacher and a Researcher with the French Naval Academy Research Institute, Lanvéoc, France. His research interests include wave propagation in complex media and signal processing. His current research focuses on ship noise from its source mechanisms to its records by ocean-bottom seismometers. His contribution to this work consisted of designing the imaging algorithm for buried object detection.

Daniel L. Orange received the B.Sc. and M.Sc. degrees in earth and planetary sciences from Massachusetts Institute of Technology, Cambridge, MA, USA, in 1985, and the Ph.D. degree in earth sciences from the University of California. Santa Cruz, Santa Cruz, CA, USA, in 1985.

After completing the Ph.D. degree, he worked entirely offshore, combining marine geology and geophysics, with a deep understanding of multibeam, to study tectonics, structural geology, geomorphology, slope failure, seepage, and process sedimentology. He has more than 23 years of industry experience in the USA and overseas, as well as academic experience primarily funded by the U.S. Navy's Office of Naval Research. Within the industry, he has applied seafloor mapping and subbottom profiling to hydrocarbon exploration and geohazards, used process geomorphology and seismic interpretation to evaluate deepwater geohazards, and applied his knowledge of survey and navigation systems to enable the successful commercialization of controlled source electromagnetics. He coauthored a book and authored/coauthored 72 peer-reviewed publications and has two patents. His contributions to this work include experiment design and data collection. His research interests include subbottom profiling away from nadir, and a comparison between latest-generation subbottom profiling and multibeam systems with legacy hull-mounted, towed, and Autonomous Undersea Vehicle systems.

Cody R. Henderson received the B.S. degrees in electrical and computer engineering and applied mathematics from Washington State University, Vancouver, WA, USA, in 2017 and the M.S. degree in signal processing and machine learning from Portland State University, Portland, OR, USA, in 2022.

He is currently an Engineer where he leverages his expertise in conducting experiments, system integration, and knowledge of underwater acoustics to develop innovative solutions for the marine industry. His contributions to this work include data collection and processing.